Home   Search   Collections   Journals   About   Contact us   My IOPscience

Electronic states at vicinal surfaces

Electronic states at vicinal surfaces

A Mugarza[1] and J E Ortega[1,2]

[1] Departamento de Física Aplicada I, Universidad del País Vasco, Plaza de Oñate 2,
E-20018 San Sebastian, Spain
[2] Donostia International Physics Centre and Centro Mixto CSIC/UPV, Manuel Lardizabal 4,
20018-San Sebastian, Spain

Abstract

Vicinal noble metal surfaces with regular arrays of steps and terraces are very convenient model systems to test the electronic properties of lateral nanostructures. Using angle-resolved photoemission with synchrotron radiation we thoroughly characterize electronic states and wavefunctions in a variety of vicinal Cu(111) and Au(111) surfaces. By tuning the terrace width, we can observe the fundamental transition from arrays of non-interacting nano-objects (terraces), where electron states are confined, to lateral coupling between terraces, which leads to superlattice states.

(Some figures in this article are in colour only in the electronic version)

1. Introduction

Vicinal surfaces with regular arrays of linear steps are among the simplest lateral nanostructures. They are particularly attractive as model systems that provide excellent playgrounds for testing the fundamental properties of electrons at one- or two-dimensional (1D or 2D) superlattices, such as wavefunctions [1–16]. The reason is that electronic states can readily be probed at the surface by powerful techniques, such as photoemission in reciprocal space [1–14] or scanning tunnelling microscopy (STM) in real space [2, 15, 16]. Vicinal noble metal (111) surfaces are particularly suitable: firstly, because they possess a free-electron-like surface state easily identified in scanning tunnelling spectroscopy and well characterized in photoemission; and secondly, because such surface electrons scatter strongly at step edges, giving rise to 1D or zero-dimensional confinement and superlattice effects.

Here we study electronic states at 1D step arrays of Cu(111) and Au(111) vicinal surfaces using angle-resolved photoemission spectroscopy (ARPES) and synchrotron radiation. Both angular resolution and photon-energy tuning allow us to probe the three-dimensional Fourier spectrum of electronic states, from which one can obtain a qualitative and quantitative description of surface state bands and electron wavefunctions. The paper is organized as follows: first we thoroughly describe the geometric structure of the noble metal vicinal
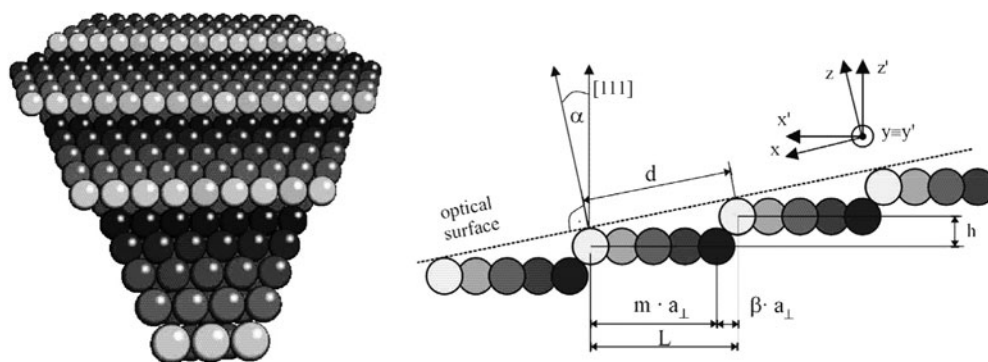
Figure 1. Schematic front view of a vicinal surface (left). Side view of the same surface, indicating the relevant parameters (right).

surfaces used in this work, focusing on the analysis of terrace width distributions (TWDs) that set the limits for reciprocal space techniques such as photoemission. Then, after giving the details of the experimental approach, we present angle-resolved, photon-energy-dependent photoemission data for a variety of vicinal surfaces with different terrace sizes from 10 to 56 Å. The results are analysed in the framework of the Kronig–Penney model for repulsive step barrier potentials. A thorough explanation of the surface state evolution in vicinal surfaces is obtained from a simplified bulk band projection picture. Finally we propose a general method for recovering real space electron wavefunctions and potential in confined systems from the photoemission data. The method is based on a phase-retrieval, iterative procedure similar to that used in x-ray diffraction.

2. Geometric structure of noble metal vicinal surfaces

Vicinal surfaces are characterized by a small tilt (miscut angle) with respect to a high symmetry (low index) plane. If the azimuthal orientation is chosen to be a high symmetry direction, the clean vicinal surface usually displays flat terraces of the high symmetry plane separated by straight steps. Due to the repulsive step–step interaction [17, 18], the latter generally appear regularly spaced, as shown in the schematic description of figure 1. The most important geometric parameters for a vicinal surface are the step array periodicity d, the terrace width L, the step height h and the miscut angle α. The optical surface is defined as the macroscopic average surface, i.e. the plane defining an angle α with the low index plane, and it is represented by dashed lines in the figure. The two relevant coordinate systems in the xz plane are also displayed: xz refers to the optical surface, whereas $x'z'$ refers to the terrace plane. Both sets of coordinates will be relevant when analysing the electronic structure.

The vicinal (111) noble metal surfaces analysed here were cut with the miscut angle perpendicular to the $[\bar{1}10]$ direction and towards either the $[\bar{1}\bar{1}2]$ or $[11\bar{2}]$ direction. Cutting in such a close-packed symmetry direction leads to straight steps by reducing kink formation. The vicinals originating from this cut display two types of different minifacets at steps, as can be seen in figure 2. In the $[\bar{1}\bar{1}2]$ direction, the minifacets are {100}-like, while in the opposite direction, i.e. $[11\bar{2}]$, the steps are {111}-like. The terrace width is slightly different for {100}- or {111}-like vicinals. Assuming periodic monatomic step arrays, terraces will contain $m + \frac{2}{3}$ atomic rows for {100}-type steps, and $m + \frac{1}{3}$ for {111}-type steps, where m is an integer number.

Vicinal Cu(111) (v-Cu(111)) surfaces were cut by spark erosion from a single crystal rod. The crystal orientation was determined by standard Laue diffraction. Using home-made tools, samples were first mechanically polished down to 0.1 μm with alumina powder, and
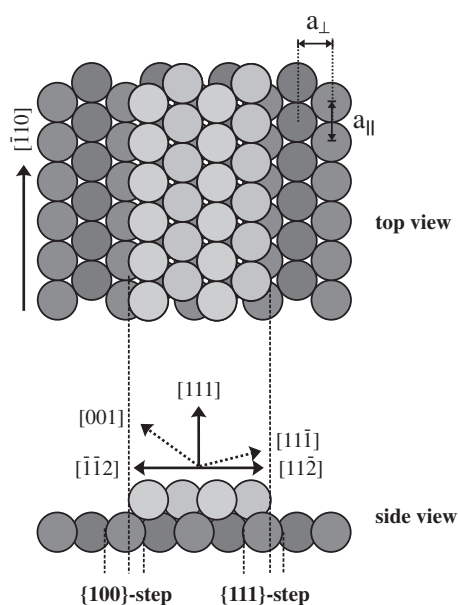
Figure 2. Top (up) and side (down) view of the vicinal (111) surface. Steps running in opposite directions display different minifacets.

then electropolished following the same procedure used for flat Cu samples [19]. The final accuracy in the miscut was better than 0.5°. The electropolishing step reduces considerably the number and duration of the sputterannealing cycles (Ar$^+$ at 500 eV, 800 K) inside the UHV system needed to obtain clean, well-ordered step arrays. Annealing, apart from recrystallizing the sputter-damaged surface, provides the steps with the mobility necessary to form a thermodynamically stable homogeneous step array. A selection of STM images for miscut angles between 5° and 11° is shown in figure 3, which corresponds to a terrace width range between 24 and 10 Å. Regularly spaced steps align vertically and only few pinning defects alter the step array. All step edges show so-called frizziness, which indicates that atoms move along the step edges. From a first analysis of the STM images it can be said that the step array becomes more regular as the miscut angle increases. This is due to the stronger step–step interaction for shorter step–step distance. The step type also seems to affect the quality of the step array. {111} steps display a more irregular array, which can be clearly observed for $\alpha \sim 5°$. For that reason we focus our analysis on vicinals with {100} steps. At this point it should be stressed that samples with the same miscut angle but different step type have been simultaneously prepared by mounting both samples together in the same sample holder with a wedge system, and measured under the very same conditions of voltage, current and scanning direction. Thus, differences in the morphology can only be related to a different step type.

For v-Au(111) we used commercial crystals (MaTeck), with an accuracy in the miscut angle of less than 0.2°. We have analysed Au(23 23 21), Au(887) and Au(223), which respectively have 2.4°, 3.5° and 11.4° miscut angles and 56, 38 and 12 Å wide terraces. Surfaces are also prepared by repeated cycles of sputtering with Ar$^+$ ions at 500 eV and annealing to 800 K. In figure 4 STM images of these surfaces are shown together with their respective TWD. The Au(111) surface is characterized by the $22 \times \sqrt{3}$ herring-bone reconstruction [20]. This reconstruction consists of fcc and hcp regions of width 38 and 25 Å, respectively, separated by a
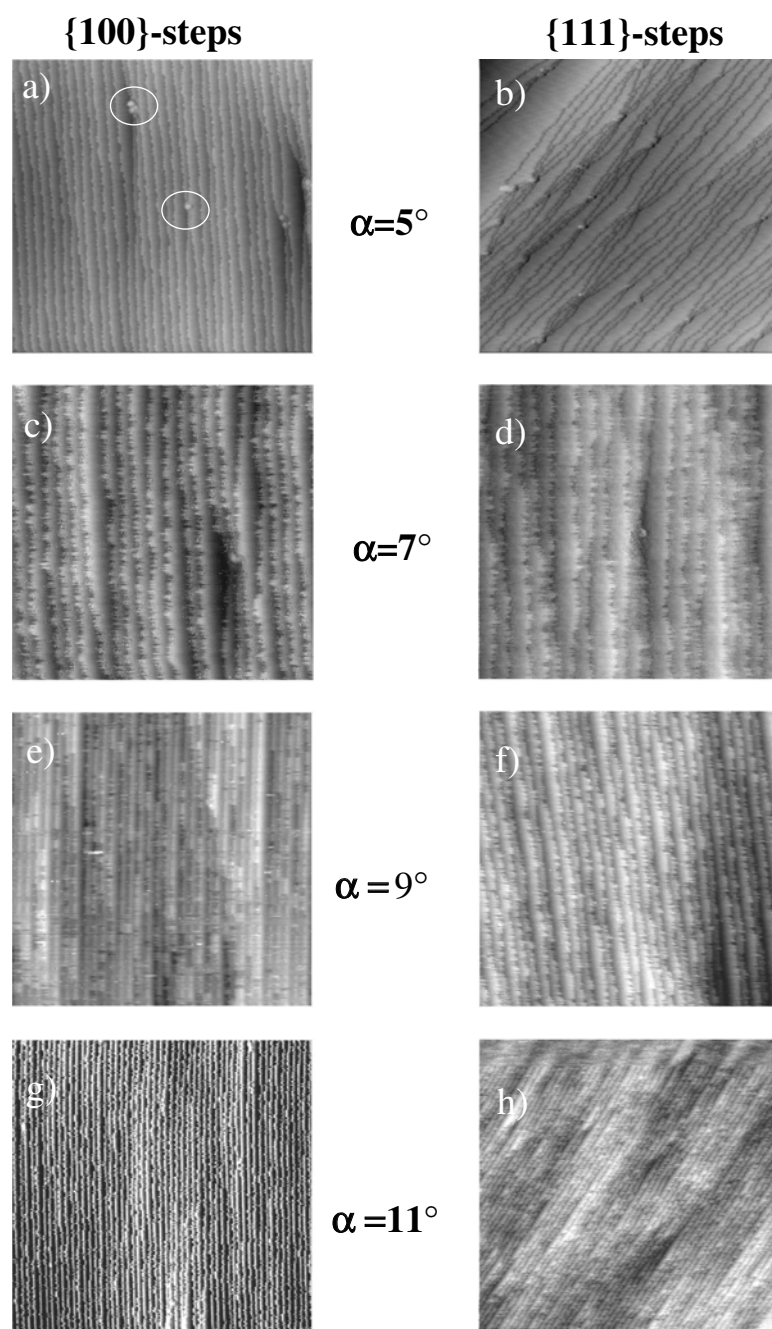
{100}-steps   **{111}-steps**

$\alpha=5°$

$\alpha=7°$

$\alpha=9°$

$\alpha=11°$

Figure 3. STM images of v-Cu(111) surfaces: (a) $\alpha = 5°$, {100} steps (750 Å)^2; (b) $\alpha = 5°$, {111} steps (750 Å)^2; (c) $\alpha = 7°$, {100} steps (350 Å)^2; (d) $\alpha = 7°$, {111} steps (300 Å)^2; (e) $\alpha = 9°$, {100}-steps (385 Å)^2; (f) $\alpha = 9°$, {111}-steps (385 Å)^2; (g) $\alpha = 11°$, {100}-steps (500 Å)^2; (h) $\alpha = 11°$, {111}-steps (500 Å)^2.

zigzag-shaped discomensuration line that protudes ∼0.2 Å. At v-Au(111) surfaces with small enough terraces and {100} steps the reconstruction is suppressed, as observed for Au(223) in

Au(223)

Au(887)
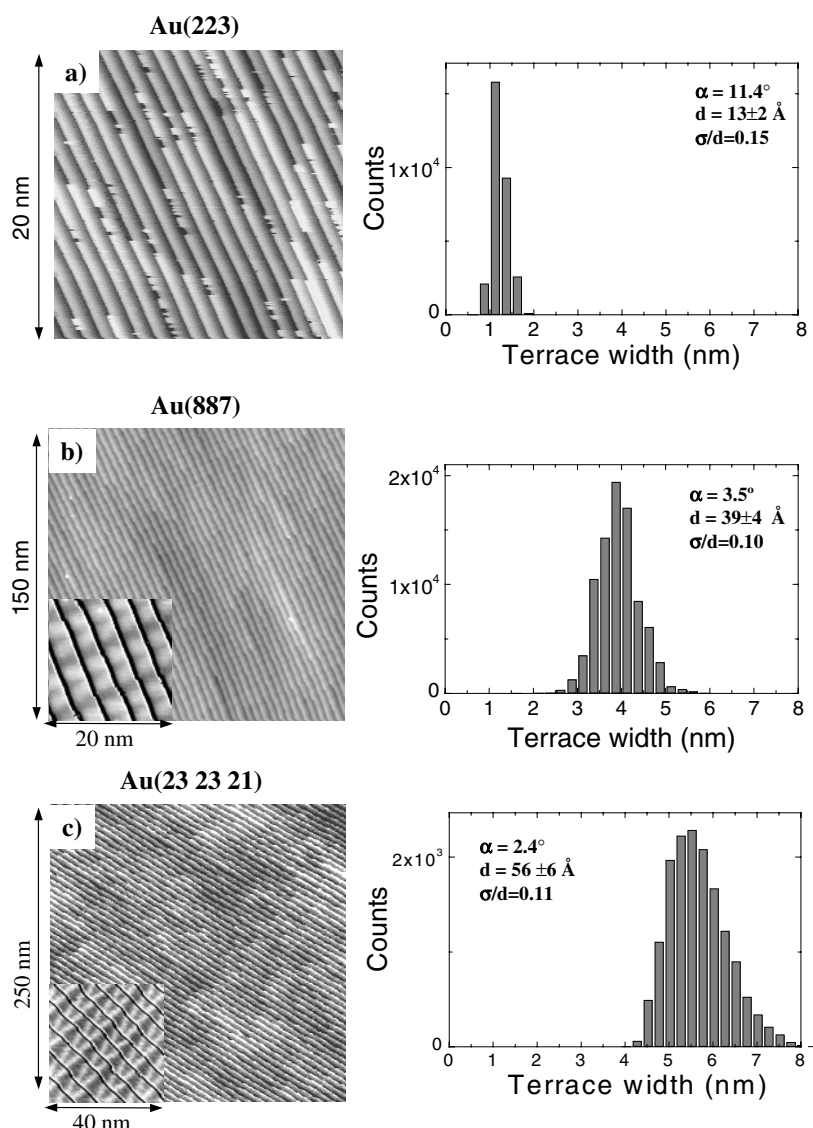

Au(23 23 21)

Figure 4. STM images of the v-Au(111) surfaces, and their respective TWDs: (a) Au(223); (b) Au(887); (c) Au(23 23 21).

figure 4(a). In this case steps appear to act as rigid boundaries and do not let the surface relax in the perpendicular direction [21]. In large terraces alternating fcc and hcp domains self-arrange parallel to step edges. Such an alternating packing displays discomensuration lines running parallel to the steps on {100}-type vicinals and perpendicular to {111}-type vicinals [21]. The latter is the case of Au(23 23 21) and Au(887), shown in figures 4(b) and (c). The reconstruction lines perpendicular to the steps are better observed in the insets of figures 4(b) and (c). The resulting corrugation along the terraces is about 0.2 Å, similar to the one found on flat Au(111). The periodicity of the reconstruction is 72 Å, slightly larger than that of Au(111) (63 Å).

The STM images in figure 4 show more regular step arrays for v-Au(111) compared with v-Cu(111), and also a relatively lower frizziness. The herring-bone reconstruction, which

Table 1. Structural parameter list for the vicinal Cu(111) and Au(111) surfaces. The values are obtained from STM image analysis. m stands for the number of atom rows per terrace. Nominal values for the Miller indices are indicated in parentheses. The terrace width deviation in the case of Cu(556), Cu(779) and Cu(223) is estimated from the miscut error, which is $\pm 0.5°$.

Vicinal index	Step type	m	α (deg)	L (Å)	$\bar{\sigma}$
Cu(556)	{100}	$10\frac{2}{3}$	5.1 (5.1)	23.6 (23.3)	—
Cu(779)	{100}	$7\frac{2}{3}$	7.3 (7.0)	16.3 (16.9)	—
Cu(557)	{100}	$5\frac{2}{3}$	8.8 (9.4)	13.2 ± 2.5 (12.6)	0.185
Cu(223)	{100}	$4\frac{2}{3}$	11.8 (11.4)	10.2 (10.3)	—
Au(23 23 21)	{111}	$22\frac{1}{3}$	2.39 (2.42)	56.5 ± 6 (55.8)	0.11
Au(887)	{111}	$15\frac{1}{3}$	3.54 (3.52)	38.9 ± 4 (38.3)	0.10
Au(223)	{100}	$4\frac{2}{3}$	10.45 (11.44)	12.8 ± 2 (11.7)	0.15

induces the faceting transition in v-Au(111) with miscut angles between ∼4° and ∼10° [21], appears to be the reason for the homogeneity and the higher stability of the v-Au(111) surfaces in figure 4. A more quantitative analysis of the step array regularity can be done by analysing the TWD σ shown in the right panels of figure 4. The values of σ obtained for all v-Au(111) and v-Cu(111) surfaces are included in table 1, where we also summarize the different parameters obtained from the STM image analysis. For v-Cu(111) the TWD was measured only for the 9° vicinal. Measurements performed by other authors with different v-Cu(111) surfaces give a value for σ between 0.2 and 0.3 [22]. Comparing the standard deviations of v-Au(111) and v-Cu(111), it can be concluded that the TWD in v-Au(111) is sharper than that in v-Cu(111) by a factor of 1.5–2.

3. Surface states at vicinal surfaces

3.1. Flat noble metal surfaces

As depicted in figure 5, surface states can be viewed as electrons confined within the surface plane due to the presence of the crystal band gap on one side and the vacuum barrier on the other. Strictly speaking, surface states originate at energy gaps of the bulk band structure projected on the surface. In (111) noble metal surfaces the projection of the s, p-bands near the Fermi level leaves a gap at the centre of the surface Brillouin zone (SBZ), as shown in figure 6. The top panel displays a cut of the bulk Fermi surface (FS) in the direction perpendicular to the surface, with the s, p-band gap arising from the L-neck projection at $\bar{\Gamma}$, i.e. at the centre of the SBZ. In the bottom panel of figure 6 we show the 2D bulk band projection over the whole SBZ. The FS of the surface state appears as a black ring centred in the gap, as expected for a 2D state with isotropic and parabolic dispersion. The surface band dispersion $E(k_\parallel)$ can be directly obtained by ARPES experiments. In particular for (111) noble metal surfaces, it has been extensively studied in the past [23–32], displaying free-electron-like isotropic behaviour parallel to the surface and around $\bar{\Gamma}$:

$$E(k_\parallel) = E_0 + \frac{\hbar^2}{2m^*}k_\parallel^2 \qquad (1)$$

where E_0 is the energy at the band bottom and m^* the effective mass. E_0 is given by the reflecting conditions of the surface–interface barriers in the perpendicular direction, whereas the effective mass m^* is related to the strength of the potential variation in the surface plane. The most accurate experimental energy dispersions (EDCs) for the three noble metals Cu,
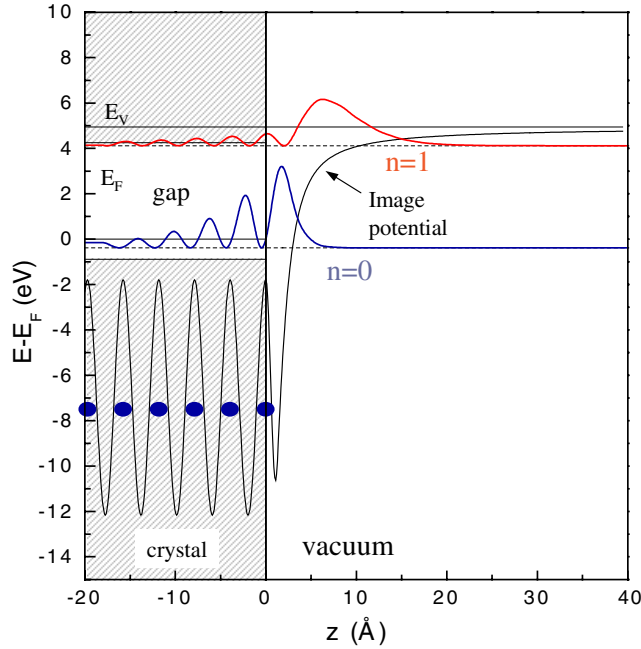
Figure 5. Potential and wavefunctions for the surface ($n = 0$) and image states ($n = 1$) in Cu(111). Surface electrons are trapped between the vacuum barrier (image potential) and the crystal gap.

Table 2. Parameters of the surface state dispersion on (111) noble metal surfaces. The energy at the band bottom, measured at $T = 30$ K, is taken from [33].

	$E_0 - E_F$ (eV)	m^*/m_e	k_F (Å^{-1})
Cu	-0.435 (-0.391[a])	0.412	0.215
Au	-0.487 (-0.440[b])	0.255	0.167/0.192
Ag	-0.063 (-0.026[b])	0.397	0.080

[a] RT values taken from [10].
[b] RT values taken from [35].

Au and Ag have been recently obtained by Reinert *et al* [33], and are displayed in figure 7. The parameters defining the dispersion are listed in table 2. As can be seen in the figure, the surface state at Au(111) is split due to the spin–orbit coupling (SOC) [31, 33]. The 2D FS of the surface state is obtained by mapping photoemission intensity distribution curves as a function of the momentum parallel to the surface, as shown in figure 7. The FS for Cu(111), Au(111) and Ag(111) is centred at $\bar{\Gamma}$ and its circular shape is an indication of the isotropic dispersion of the surface state. The radius depends on both the band bottom and the effective mass. In Au(111) the SOC splits the FS in two concentric rings. The spin of each ring is azimuthal, rotating in opposite directions. The broader FS in Ag(111) has also been attributed to a smaller, unresolved SOC splitting [34].

3.2. Vicinal noble metal surfaces

As frequently observed in STM, the s, p-like surface state of (111) noble metal surfaces is very sensitive to adsorbates (adatoms), vacancies and surface steps, where surface electrons
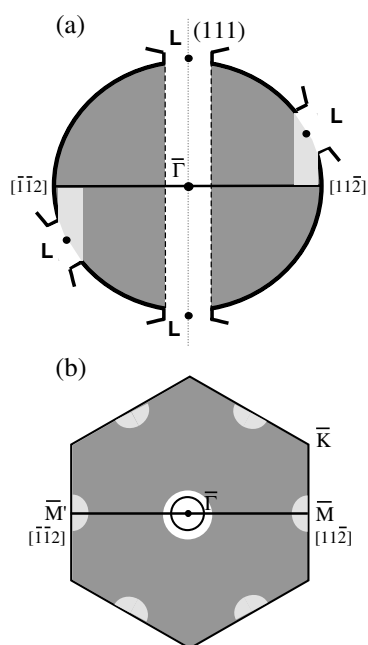
Figure 6. (a) Vertical cut in the (k_x, k_z) plane, showing the projected bulk bands at the Fermi energy. A gap is formed at the centre of the SBZ. (b) A 2D view of the SBZ with the circular gap centred at $\bar{\Gamma}$. The Fermi surface of the surface states appears as a ring centred in the gap.

scatter strongly [15, 16, 36–39]. Thus a regular array of surface scatterers, like the 1D step array of the vicinal surface, is expected to modify the surface band dispersion deeply, leading to electron confinement and superlattice effects. The latter can be appropriately measured by angle-resolved photoemission, which also provides an interesting insight into wavefunctions [6, 8, 12–14].

In the following we present a thorough description of surface states at noble metal vicinal surfaces using the variety of crystals described above. The photoemission experiments were performed with tunable synchrotron radiation at LURE (Paris), HASYLAB (Hamburg) and SRC (Wisconsin) facilities. Experiments on v-Cu(111), Au(223) and Au(887) were done at 300 K using p-polarized light at LURE and HASYLAB, where the experimental stations are equipped with conventional angle-resolved photoemission setups that provide angular resolution around 0.5° and total energy resolution of 50 meV. The measuring geometry for the dispersion perpendicular to the steps is sketched in figure 8. The emission plane contains both the incident light and the photoelectron, and the emission angle is selected by turning the analyser. At SRC we analysed the case of Au(23 23 21) at 120 K, using a Scienta SES200 spectrometer with an angular resolution of 0.3°, total energy resolution of 10 meV and also p-polarized light. The Scienta angle is set perpendicular to the step array. In this case the experimental setup was such that the incident light was perpendicular to the emission plane.

In figure 9 we show the photoemission spectra for Au(23 23 21) and Cu(11 11 9) with varying emission angle in the direction parallel to the steps. The spectra are dominated by the intense surface state peak near the Fermi level. In Au(23 23 21) the peak splits at higher emission angles due to the SOC (tick marks in the figure), in the same way as observed in flat Au(111) [31, 34]. For a quantitative analysis of the band dispersion we obtain electron
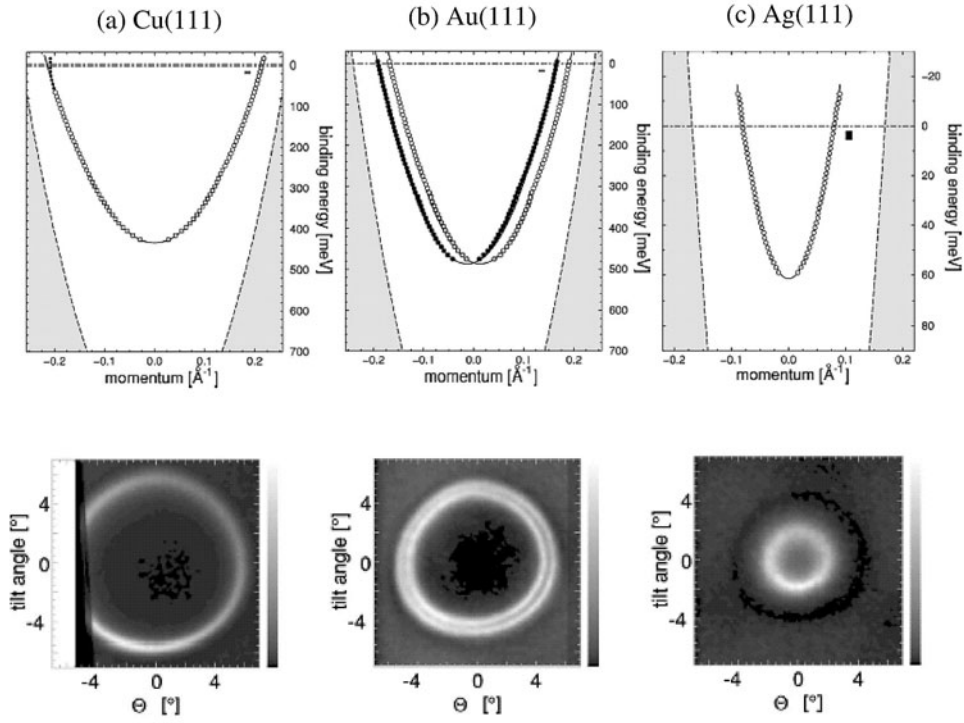
Figure 7. Surface bands (top) and FS (bottom) of (a) Cu(111), (b) Au(111) and (c) Ag(111). The shaded areas in the top panels correspond to the bulk band projections. The circular shape of the FS reflects the isotropic dispersion parallel to the surface. In the case of Au(111), the surface state band splits due to the SOC, which leads to two concentric rings in the FS (adapted from [33]).
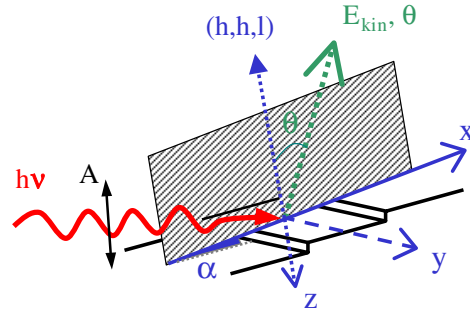

Figure 8. Measurement geometry in angle-resolved photoemission for surface band dispersion perpendicular to the steps. The shaded area represents the emission plane that contains both photons and electrons. In the case of Au(23 23 21) the experimental setup was such that the incident light was perpendicular to the emission plane.

energies from the peak maxima and parallel wavevectors from the emission angle θ and the measured electron kinetic energy E_{kin} by using the known formula [40]

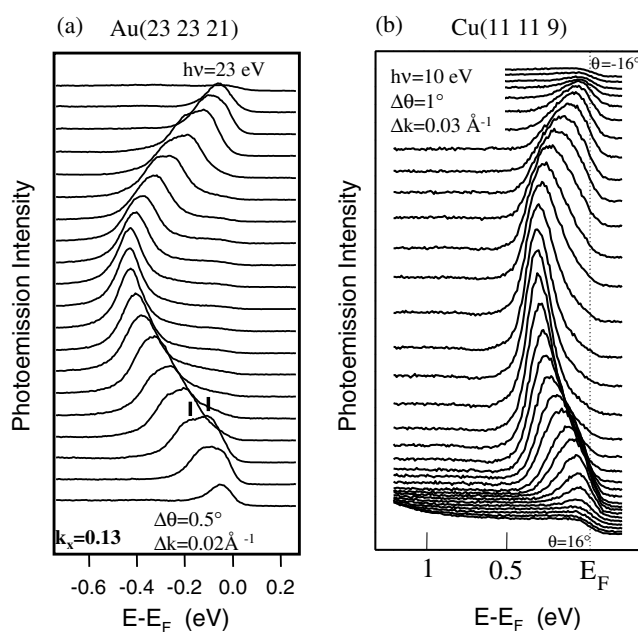$$k_{x,y} = \sqrt{\frac{2m E_{kin}}{\hbar^2}} \sin\theta. \tag{2}$$

Figure 9. Dispersion of the surface state in the direction parallel to the steps at (a) Au(23 23 21) and (b) Cu(11 11 9). The parabolic dispersion indicates the free-electron-like behaviour along the terraces. The ticks in the left figure indicate the SOC splitting, similar to that observed in flat Au(111).

The data obtained from the spectra in figure 9 can be fitted to free-electron-like parabolas with effective mass of $m^* = 0.254\, m_e$ for Au(23 23 21) and $m^* = 0.46\, m_e$, very similar to the latest photoemission results on Au(111) and Cu(111) [34, 35]. In both cases the minimum of the parabola is at $k_y = 0$, as observed for flat crystals. In order to extract the spin–orbit splitting in Au(23 23 21) it is possible to refine the analysis of the spectra including a line fit with a double peak. This leads to two parabolic bands, with the same k_y-dependent split found in flat surfaces [13]. Thus the same dispersion and SOC splitting of the flat surface are found in the stepped one along the parallel direction, and hence we conclude that parallel to the terraces the electronic structure remains unaltered by the step array.

By contrast, the surface electronic structure is strongly modified in the direction perpendicular to the steps. In figure 10 we show the EDC curves in the direction perpendicular to the steps for the three Au vicinals. The emission angle is taken relative to the optical or average surface (see figure 8). The photoemission spectra were obtained at a photon energy $h\nu = 27$ eV for Au(223) and Au(887) and at $h\nu = 60$ eV for Au(23 23 21). A remarkable difference is observed between Au(223), i.e. the surface with 12 Å wide terraces, and Au(887) and Au(23 23 21), with 39 and 56 Å wide terraces respectively. A broad, 2D dispersing feature is observed in Au(223), whereas the surface state splits into sharp non-dispersing peaks in Au(887) and Au(23 23 21) (indicated by dashed lines). The intensity of the latter is modulated along the emission angle and the number of split peaks depends on the terrace width: two peaks are observed in Au(887), which has the narrowest terraces, and three in Au(23 23 21). A colour plot of each EDC spectra series is shown below, where the horizontal axis stands for the emission angle and the vertical axis for the energy. Both the energy and the angular dependence of the photoemission intensity of the non-dispersing peaks are directly observed in such colour plots. In Au(223) we observe a double parabolic dispersion, away from normal
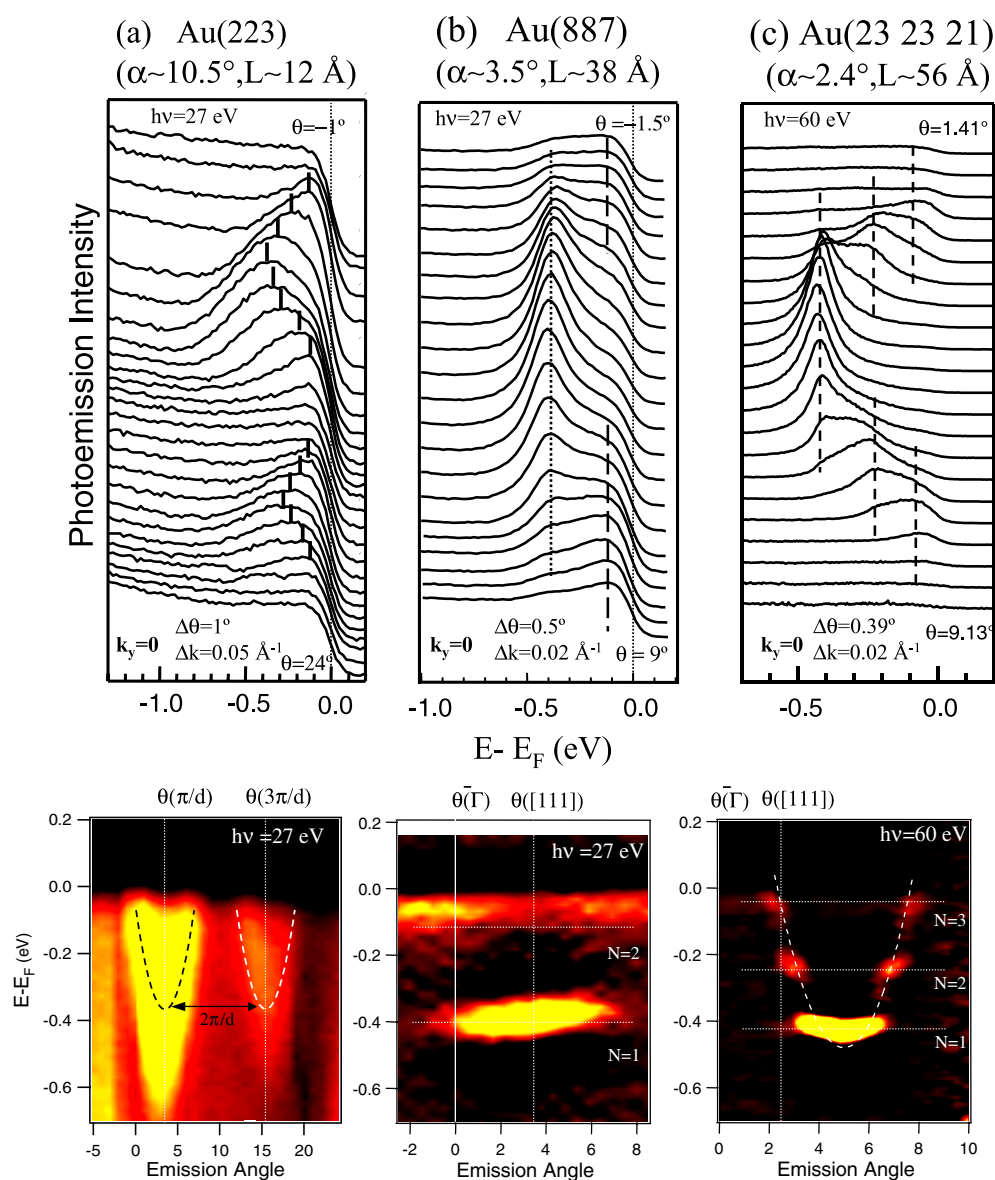
Figure 10. Series of EDC curves in the direction perpendicular to the steps for (a) Au(223), (b) Au(887) and (c) Au(23 23 21). In Au(223) the surface state is a duplicated broad 2D dispersing feature while in the other two vicinals the surface state splits into sharp 1D non-dispersing peaks (dashed lines). The figures at the bottom are colour-scale plots of the same series. For (b) and (c) the second energy derivative of the EDC spectra is used to enhance the peak features.

emission and shifted up in energy with respect to flat Au(111). In order to enhance the different features, in the case of Au(887) and Au(23 23 21) we have plotted the second energy derivative of the spectra. The latter is proportional to the peak intensity for constant peak width [41].

In Cu(111) vicinals, the surface state displays parabolic dispersion for all terrace widths. Figure 11 shows the angle-resolved measurements in the direction perpendicular to the steps for Cu(223), Cu(557) and Cu(556), with 10, 13 and 24 Å wide terraces, respectively. As in the
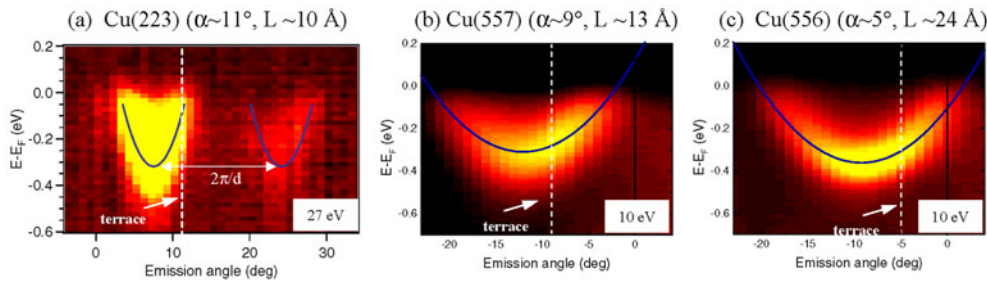
Figure 11. Surface band dispersion perpendicular to the surface for (a) Cu(223), (b) Cu(557) and (c) Cu(556). A parabolic dispersion can be observed in the three cases, where the energy as well as the momentum of the band centre are shifted with respect to Au(111). For Cu(223) the parabola is duplicated.
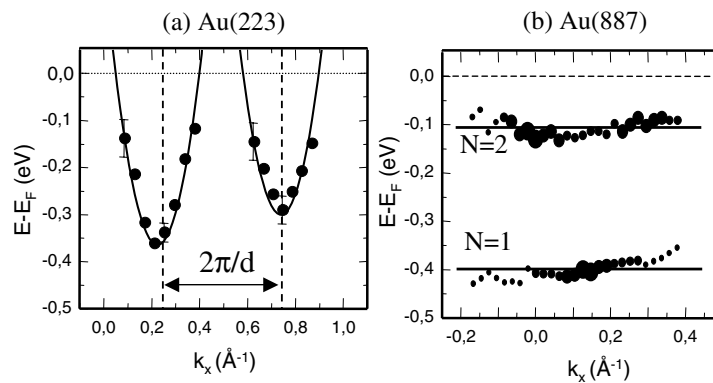

Figure 12. $E(k_x)$ surface bands. (a) In Au(223) the surface state forms superlattice bands, zone folded by the superlattice vector $g = 2\pi/d$. (b) In Au(887) two 1D quantum well (QW) levels are observed. The size of the dots is proportional to the corresponding peak intensity in figure 10. The energy gap between QW levels in Au(887) is consistent with confinement within terraces.

case of Au(223), the peaks appear broadened compared with those observed on the flat surface. The band bottom is also shifted in energy and emission angle with respect to the flat surface. In the case of Cu(223) the parabola is also duplicated, similar to Au(223). The absence of a double band in Cu(557) and Cu(556) is simply due to the low photon energy used in both cases. As we show later, the particular Fourier spectrum of the surface state at vicinal surfaces limits the observation of duplicated bands only within a narrow photon energy range.

For a quantitative analysis, in the case of v-Cu(111) and Au(223) we obtain the surface band dispersion from the peak maxima in the EDC spectra. For Au(887) and Au(23 23 21), due to the overlap of the different features, it is convenient to perform a line fitting to individual spectra. Following the standard procedure, we used Lorentzian peaks, Shirley and smooth backgrounds, and Gaussian convolution to account for the experimental resolution. These allow a clear identification of the different non-dispersing levels, as well as the peak intensity for further analysis (see below). As an example we show the resulting dispersion relations for the case of Au(223) and Au(887) in figure 12. k_x is assumed to be positive in the step-up direction. The slight upward energy shift of the second parabola is only an artefact related to its relatively weak intensity at this particular photon energy. The energy shift disappears at photon energies where both parabolas show similar intensities (not shown here). We can locate
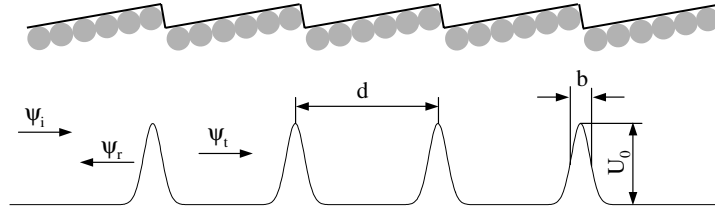
Figure 13. Kronig–Penney potential mimicking the potential array formed by the step superlattice.

the two parabolas in momentum space at $k_x = 0.23 \pm 0.04$ and 0.74 ± 0.04 Å^{-1}. The distance between the two parabolas is $\Delta k_x = 0.51$ Å^{-1}. This value is close to the reciprocal vector $g = 2\pi/d = 0.49$ Å^{-1}, suggesting band folding by the step superlattice. Zone-folding effects can only take place in the presence of a finite periodic potential that allows coupling from terrace to terrace. The upward energy shift relative to the case of a flat surface indicates the repulsive nature of the step barrier. In contrast, for Au(887) we clearly observe two flat levels at -0.40 and -0.11 eV, rather indicating strong confinement along the k_x direction.

3.3. Analysis within the Kronig–Penney model

The overall changes in the surface electronic structure induced by the step array can be properly analysed within the framework of the 1D Kronig–Penney (KP) model [2, 10]. The step lattice can be viewed as a periodic array of potential barriers, as described in figure 13. Little is known about the shape of the step potential but, according to calculations done within the jellium model [42], it seems to be located over a range of a few angstroms on either side of the step. Nevertheless, the barrier can be simplified by choosing a δ-Dirac barrier $U_0 b \delta(x)$, hence disregarding the shape and width of the step potential. Indeed, it has been shown that one can always replace a potential barrier by a suitably chosen δ function [43], although the strength $U_0 b$ depends on the energy. Since the energy range we are interested in is small, taking U_0 as a constant should be a good approximation [44]. As for any other periodic potential, the KP model gives bands and forbidden gaps as solutions of the energy dispersion. For a potential consisting of a periodic array of δ functions, i.e. $V(x) = \sum_n U_0 b \, \delta(x - nd)$, the dispersion relation takes the following form:

$$E(k_x) = E_0 + \frac{\hbar^2}{2m^*} \frac{1}{d^2} [\cos^{-1}(|T| \cos k_x d) - \phi]^2 \tag{3}$$

where E_0 is the energy at the band bottom when $d \to \infty$, i.e. for a terrace of infinite width. $|T|$ is the modulus of the transmission coefficient and ϕ the phase. Both can be expressed as

$$|T|^2 = \frac{1}{1 + (q_0/q)^2} \tag{4}$$

and

$$\phi = -\tan^{-1}(q_0/q) \tag{5}$$

where $q_0 = (m^*/\hbar^2) \cdot U_0 b$ and $q = \sqrt{(2m^*/\hbar^2)(E - E_0)}$. Note that for an infinite barrier, i.e. $U_0 b = \infty$, $|T| = 0$ and $\phi = -\pi/2$, which corresponds to a phase shift in the wavefunction of $\pm \pi$. Then we recover the expression of the energy for an infinite well:

$$E_N = E_0 + \frac{\hbar^2}{2m^*} \frac{\pi^2}{d^2} N^2 \qquad \text{for} \quad N = 1, 2, 3 \ldots . \tag{6}$$
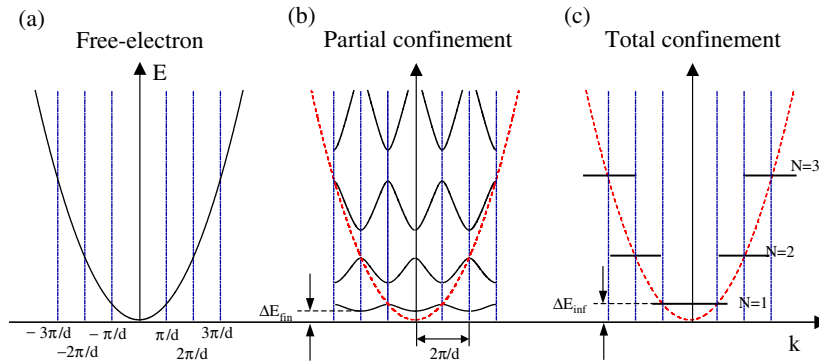
Figure 14. KP bands for increasing potential barrier. (a) $U_0 b = 0$, free-electron parabola. (b) Finite potential barrier. The band splits into superlattice subbands which are zone folded by the reciprocal superlattice vector $g_n = 2\pi/d$. (c) Infinite potential barrier. The subbands become flat levels. The levels are centred at $k = \pi/d \cdot N$ (except $N = 1$, see text) where N stands for the Nth energy level. The free-electron parabola is plotted in (b) and (c) in red.
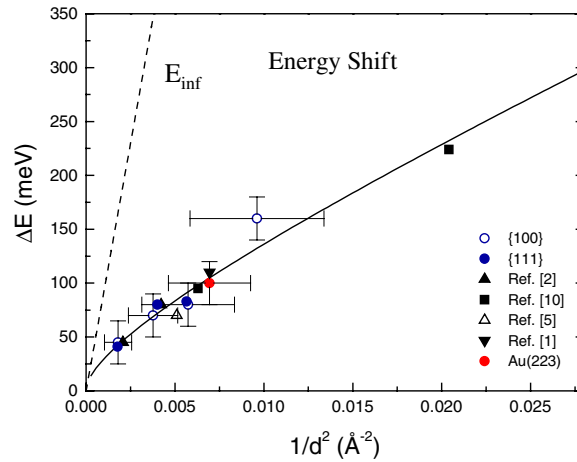

Figure 15. Energy shift as a function of $1/d^2$ for different Cu and Au vicinals. The solid curve is obtained by inserting the linear fits of $|T|$ and ϕ of figure 16 in equation (7). The dashed line represents the energy shift for the case of an infinite barrier.

On the other hand, for $U_0 b = 0$, $|T| = 1$ and $\phi = 0$, and equation (3) reduces to the free-electron-like band described in equation (1).

The energy dispersions for these three different cases are displayed in figure 14. The free-electron parabola splits into superlattice subbands in the presence of a finite potential, which are zone folded by the superlattice vectors $g_n = 2\pi/d \cdot n$. As we increase the potential barrier the gaps become wider and the subbands flatter. In the limiting case of an infinite barrier, the bands become flat energy levels. The momentum distribution of the Nth energy level is centred at $k_x = \pi/d \cdot N$ in analogy to the 2D QW energy levels of thin films [45], except the $N = 1$ level. In the latter the QW only contains a half-wavelength of the sine function, which is not enough to centre the Fourier transform at its period $k_x = \pi/d$. The resulting Fourier distribution is centred at $k_x = 0$.

For dispersing surface states in v-Cu(111) and Au(223), we can obtain the transmission probability and the barrier strength by fitting the experimental energy shift ΔE at the centre of the band using equation (3), which takes the following form for $k_x = 0$:

$$\Delta E(d) = E(0) - E_0 = \frac{\hbar^2}{2m^*} \frac{1}{d^2} \left[\cos^{-1}\left(\frac{1}{\sqrt{1 + (q_0/q(\Delta E))^2}} \right) + \tan^{-1}(q_0/q(\Delta E)) \right]^2. \quad (7)$$

q_0 is obtained from this fit and hence the potential barrier $U_0 b$, the transmission probability $|T|^2$ and the phase ϕ. In figure 15 data points represent the experimental values of the energy shift $\Delta E(d)$ of the surface state band at v-Cu(111) and v-Au(111) plotted as a function of $1/d^2$. We also include results for Cu vicinals reported in the literature. The deviation of the experimental values from the case of the infinite barrier (dashed line) is clear from this plot. The corresponding values of $|T|^2$, ϕ and $U_0 b$ are shown in figure 16. The data are fitted with straight lines, which in turn are used to obtain the analytical (empirical) expression for $\Delta E(d)$ shown in figure 15 as a solid curve. The transmission probability in figure 16 increases with decreasing terrace width and it is considerably high for all cases, lying between 0.6 and 0.8. The phase is also far from that corresponding to total confinement, i.e. $\pm \pi$, as could be deduced from the transmission. Finally, the potential barrier also increases for decreasing terrace width, going from 1 up to 1.5 eV Å. Changes in the elastic stress at steps as a function of terrace width or the interaction between line dipoles of neighbouring steps could in fact slightly modify the potential barrier. Also the overlap of surface and bulk states is expected to change due to different bulk band projections on each vicinal surface, thereby affecting the effective potential barrier at the step. This point is discussed later, since it appears to be the reason for the transition from non-dispersing, confined states at wide terraces to superlattice dispersing bands at vicinal surfaces with narrow terraces.

The peak fitting for Au(887) and Au(23 23 21) leads to the energy levels listed in table 3 together with the standard deviation. The proximity to the Fermi level did not allow the calculation of the standard deviation for the $N = 3$ level at Au(23 23 21). The standard deviation found for all non-dispersing energy levels falls below 50 meV. Therefore, there is a strong electron confinement and consequently negligible transmission or coupling across the step barriers. The energy levels lie lower and the gap between them is smaller for Au(23 23 21), where the terrace width is higher. The results are generally consistent with confinement in a 1D QW of size L, where L is the terrace width[3]. Furthermore, as shown in figure 17, all quantum levels in Au(23 23 21) and Au(887) fit nicely to those of the infinite QW, given by

$$E_N = E_0 + \frac{\hbar^2}{2m^*} \left(\frac{\pi}{L} \cdot N \right)^2. \quad (8)$$

In figure 17 the straight fit to data points for both Au(23 23 21) and Au(887) assumes the same effective mass $m^* = 0.255\, m_e$ of the flat surface and uses a unique reference energy E_0 as the fitting parameter. The deviation between the experimental energy levels and the infinite QW in Au(23 23 21) is below 30 meV and the average is 16 meV, indicating a very good agreement. We obtain $E_0 = -0.48$ eV, which lies within the range of the reported values for the band bottom of the surface state on Au(111) [31, 33, 35, 46].

The photoemission intensity from the QW spectra in figure 10 appears broadened in the emission angle (k_x) and the energy scale. Both result in the intensity modulation that tends to track the free-electron-like parabola. Wavevector broadening is naturally explained by terrace confinement in real space. Furthermore, a refined analysis of the k_x-dependent

---

[3] For the small miscut angles used in this work L and d differ by less than 0.02%. In any case, L rather than d should be considered as the terrace confinement length.
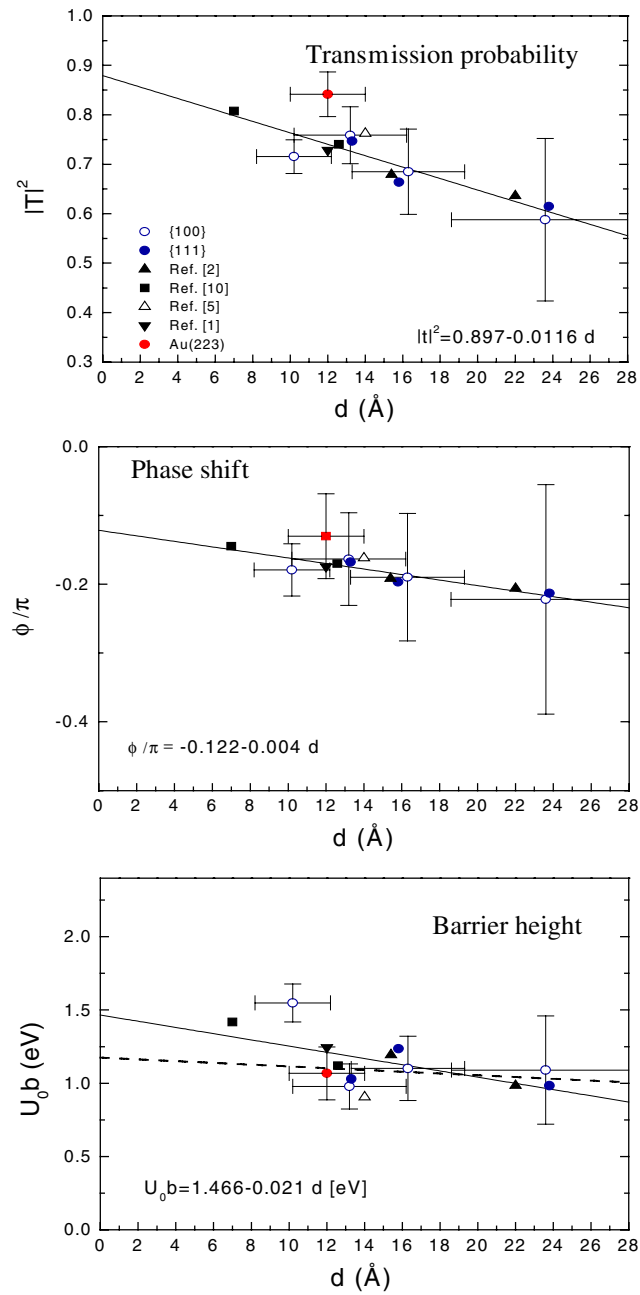
Figure 16. Transmission probability, phase of the transmission coefficient and barrier height as a function of terrace width. The transmission probability and the phase are calculated for the band bottom. The data are fitted with a linear function (solid line).

intensity is used to obtain the electron wavefunction in the QW, as we show later. The energy broadening, which is quantified in table 3 by the standard deviation of the different energy levels, can be due either to the existence of a slight band dispersion or to TWD effects.
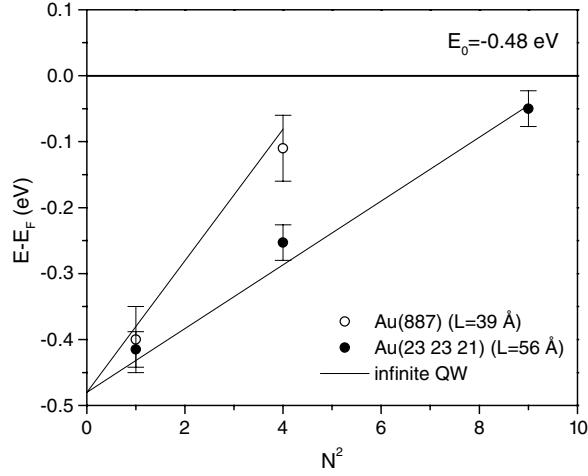
Figure 17. Fit of the QW levels in Au(887) and Au(23 23 21) with the infinite QW model. Both sets of data points are simultaneously fitted with the same $E_0 = -0.480$ eV.

Table 3. Energy levels obtained in the fit of the EDC spectra for Au(887) and Au(23 23 21). The values in parentheses are the energy levels obtained from the infinite QW model with reference energy $E_0 = -0.480$ eV. The standard deviations ΔE of the fitting are also listed. ΔE_3 for Au(23 23 21) has not been calculated, since the proximity of the Fermi level did not allow a proper measurement.

Vicinal	E_1 (eV)	E_2 (eV)	E_2 (eV)	ΔE_1 (eV)	ΔE_2 (eV)	ΔE_3 (eV)
Au(887)	−0.400 (−0.380)	−0.110 (−0.81)	—	0.015	0.038	—
Au(23 23 21)	−0.427 (−0.432)	−0.274 (−0.287)	−0.060 (−0.45)	0.027	0.041	—

First we consider such standard deviation as due to the residual dispersion of the superlattice subbands with multiple zone foldings along k_x, i.e. the mini-bandwidth. Using the KP model we estimate the maximum transmission through the steps in Au(23 23 21) and Au(887). At the $N = 1$ level, which corresponds to the band bottom in a superlattice state, the resulting maximum transmission probabilities are $|T|^2_{max} = 0.008$ and $|T|^2_{max} = 0.026$ for Au(887) and Au(23 23 21) respectively. At $E = -0.100$ eV, i.e. near the highest observable energy level below E_F for both surfaces, the transmission probability is $|T|^2_{max} = 0.035$ and $|T|^2_{max} = 0.18$ for Au(23 23 21). Within the simple KP model, such transmission probabilities lead to step potential barriers $U_0 b$ of 25 and 10 eV Å, respectively. Thus, assuming a small subband dispersion, we obtain a very high step barrier potential that has no physical meaning. This suggests that the analysis based on the simple KP model is limited. So far we have neglected inelastic scattering (absorption) at steps, i.e. complex step barrier potentials. As a matter of fact, a smaller real potential with a large imaginary part due to strong absorption could display the same energy levels of the infinite QW. Indeed, significant absorption by surface–bulk mixing is theoretically predicted and experimentally observed with STM in the lateral confinement of surface states by steps, adsorbate rows or adatom corrals [15, 16, 36–39, 47–49]. No observable differences between the energy levels obtained in these works and that of the infinite QW are found, which is ascribed to the lack of transmission (the slight energy differences observed in [49] are below our experimental resolution).
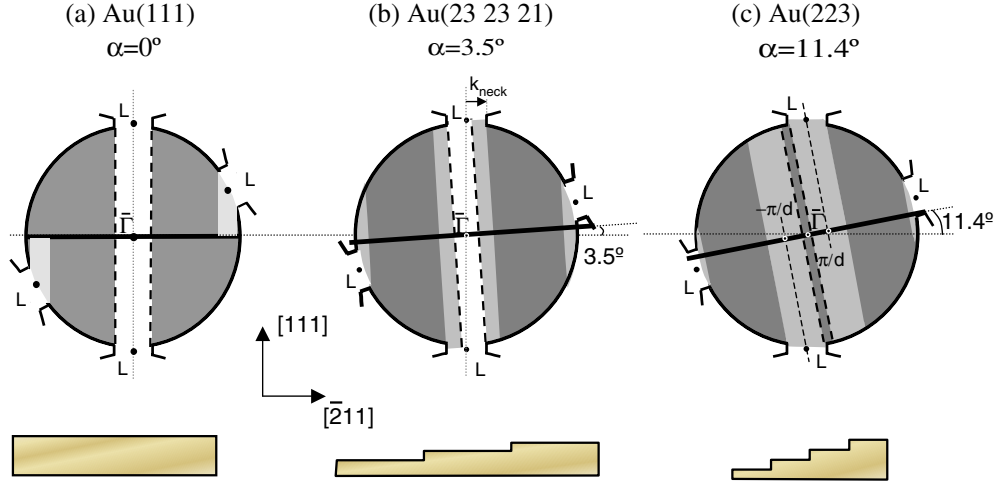
(a) Au(111)
α=0°

(b) Au(23 23 21)
α=3.5°

(c) Au(223)
α=11.4°

Figure 18. Bulk band projection at $E = E_F$ onto vicinal surfaces with small and high miscut angles in the xz plane. Dark-grey zones are the regions where bands are projected from both sides of the BZ, whereas light-grey zones present projection only from half a side. For 3.5°, the $\bar{\Gamma}$ gap that supports the L-neck surface state is still present. For 11° miscut there are bulk states projected over the entire SBZ and only surface resonances can exist.

On the other hand, the energy broadening of the QW levels due to a finite TWD can be estimated as

$$\Delta E = \frac{\hbar^2}{2m^*} \frac{2\pi}{L^3} \Delta L \; N^2 \tag{9}$$

where ΔL is the TWD. Using the STM values of table 1, we obtain values of $\Delta E_1 = 25$ and $\Delta E_2 = 100$ meV for Au(887) and $\Delta E_1 = 10$ meV, $\Delta E_2 = 40$ meV and $\Delta E_3 = 90$ meV for Au(23 23 21). These are similar to the standard deviations shown in table 3, and suggest that TWD is rather the dominating source of energy broadening of the QW levels in figure 10.

4. 1D versus 2D surface states

One general conclusion from the KP analysis is that the 1D or 2D nature of the s, p-like surface state at vicinal surfaces with large or small surfaces, respectively, can only be explained by assuming a considerable change in the effective step potential that the electron feels as a function of the miscut angle. The large step barriers found for Au(23 23 21) and Au(887) are not compatible with the small quantum size shifts found for the rest of the surfaces. As mentioned above, we expect the step potential to become smoother at narrow terraces due to the overlap of the line dipoles of neighbouring steps [42]. However, the step potential extends approximately ±2 Å around the steps, and hence significant smoothing is expected only at terraces with one to two atomic rows.

On the other hand, by changing the miscut angle the band structure projection of the flat surface shown in figure 5 does not hold. The surface plane rotates and hence the band projection along the SBZ. This is schematically depicted for different miscuts in figure 18. In this figure, the surface plane is represented by the thick black line that rotates with the miscut angle. Along this plane, regions of the SBZ where bulk bands are projected from both sides of the BZ are marked in dark grey, whereas regions with projection only from half of the BZ are marked in light grey. The L-point projection marks the edge of the SBZ at $\pm\pi/d$. Our interest
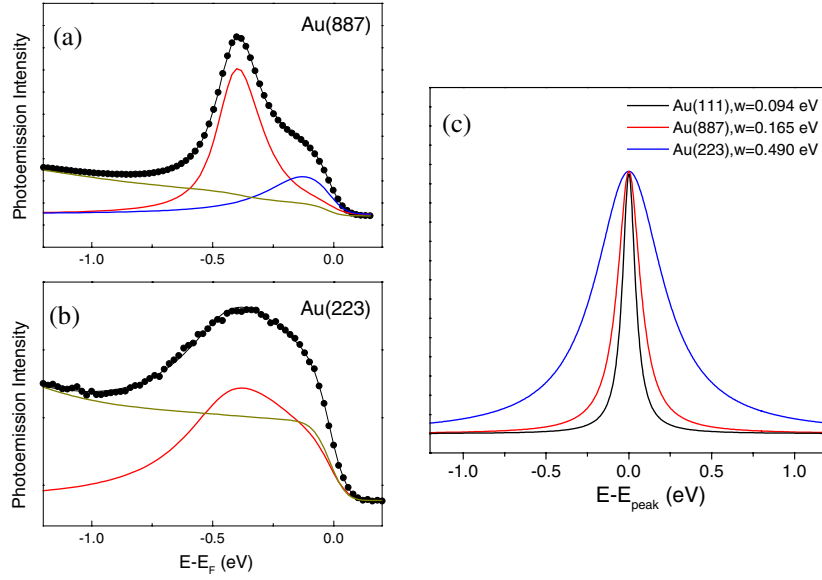
Figure 19. Fit of the EDC curves for (a) Au(887) and (b) Au(223). (c) The resulting Lorentzian at the band bottom for Au(223) and Au(111) and at the $N = 1$ maximum for Au(887).

is focused on the projected gap that supports the surface state. For the 3.5° miscut, the gap is narrower than in flat Au(111) but still exists in the centre of the SBZ. By increasing the miscut angle the $\bar{\Gamma}$ gap shrinks and eventually vanishes. As shown in the figure, for Au(223) with 11° miscut there are bulk states projected over the whole SBZ and no $\bar{\Gamma}$ gap. The critical miscut for closing the gap is easily obtained as $\alpha_c = \tan^{-1}(k_{\text{neck}}/k_L)$, where k_{neck} is the radius of the neck and k_L is the distance $\overline{\Gamma L}$. For Cu, $k_{\text{neck}} = 0.19$ and 0.26 Å^{-1} for the band bottom and E_F respectively, and for Au $k_{\text{neck}} = 0.18$ and 0.24 Å^{-1}. These values lead to closing angle ranges of $\alpha_c \sim 7.2°$–$9.8°$ for Cu and $\alpha_c \sim 7.7°$–$10.2°$ for Au.

Strictly speaking, surface states can only exist in the presence of a gap; thus the peaks observed for miscut angles bigger than α_c will be surface resonances. The increasing overlap with bulk states manifests itself in the surface state peak width. In figures 19(a) and (b) we show the spectra at the surface band minimum in Au(223) and the $N = 1$ level for Au(887). For the latter we have chosen the spectrum with maximum intensity, i.e. at the centre of the angular distribution. By applying the fitting procedure explained above we obtained the Lorentzian surface peaks shown in figure 19(c) for both Au(223) and Au(887). In this figure we also include as a reference the corresponding Lorentzian peak for flat Au(111), assuming a width of $w_{111} = 94$ meV that results from the convolution of the 50 meV Lorentzian lifetime broadening [50] plus the 80 meV experimental Gaussian width. The $N = 1$ level for Au(887) has $w_{887} = 165$ meV, which is about twice the width of the surface state on flat Au(111), whereas for Au(223) we obtain $w_{223} = 490$ meV, i.e. three times bigger than in Au(887). After subtracting the TWD contribution (15 meV for Au(887) and 100 meV for Au(223)), as well as the experimental resolution, we obtain a lifetime broadening of 143 meV in Au(887) and 330 meV in Au(223). The difference can be explained, within the band projection picture of figure 18, as due to the absence of a projected band gap in Au(223), which permits only surface resonances in this case.

Since resonances are coupled to bulk states they are less confined to the surface than real surface states. Thus surface resonances are effectively found deeper in the bulk, and hence

less affected by the step potential. The latter becomes smoother as we enter the bulk, as shown in figure 20(a). There we show the electrostatic potential induced by the dipole-like charge-density formation at the step edge, as calculated by Wang *et al* [5]. In the direction perpendicular to the surface, the potential barrier diminishes rapidly, decreasing to ∼50% for 2 Å inside the bulk. Figure 20(a) indicates that the effective step potential barrier will dramatically depend on the localization of the electron in the direction perpendicular to the surface. As shown in figure 20(b), the effective potential barrier can be estimated from the overlap between the electron probability density and the step potential in the direction perpendicular to the surface:

$$V_{\text{eff}}(x_0) = \int V(x_0, z)|\varphi(z)|^2 \, dz \tag{10}$$

where x_0 can be chosen to be the step edge. For numerical estimations we can assume a 2 Å wide Gaussian step barrier $V(x_0, z)$ along the z direction, and an exponentially damped Bloch wavefunction for the surface resonance, with decay length λ. The reduction in the effective step potential is already quite strong for rather small decay lengths. In figure 20(b) we show two different examples. The penetration of a real surface state on Au(111) is around 2.5 ML, whereas larger penetrations between 9 and 20 ML are typical for resonances [58] or surface states near gap edges [51]. Compared with the potential value $V(x_0, 0)$ at the step, the effective potential $V_{\text{eff}}(x_0)$ reduces to $0.5 \cdot V(x_0, 0)$ for $\lambda = 2.5$ ML, to $0.2 \cdot V(x_0, 0)$ for $\lambda = 9$ ML, and to $0.1 \cdot V(x_0, 0)$ for $\lambda = 20$ ML. Thus, a decrease in the effective potential by a factor of 2.5–5 seems reasonable in the transition from 1D QW states to 2D superlattice states.

Although our result is independent of the shape and value of the step potential $V(x, z)$, little is known about it. Full atomistic scattering calculations of different adsorbates on Cu(111) show strong similarities between their scattering properties [49], which in our case would be represented by the complex step potential. Similar scattering properties are also found for different confining elements analysed by other authors [15, 16, 36–39, 47, 48]. Thus, the common transition miscut angle observed for v-Cu and v-Au could be explained by both the similar bulk band projection and step potentials in these surfaces.

5. Terrace versus average-surface character

Due to total confinement, 1D QW states can be defined as terrace-like states, since they do not 'see' the average, stepped surface. By contrast, 2D surface states propagate across the surface plane, which differs from the terrace by the miscut angle. Thus one can define a distinct terrace or average-surface character or modulation plane for the surface state wavefunction. Such character can be probed in photon-energy-dependent photoemission experiments. The data for Au(223) and Au(23 23 21) are shown in figures 21(a) and (b). Both surfaces display duplicated spectra that change their relative intensity as we tune the photon energy. The situation resembles that of electron diffraction from a stepped surface, shown in figure 21(c), where the split spots are only observed in anti-phase interference conditions [52]. Furthermore, the spectra in figure 21(c) correspond to the (00) spot at normal incidence, and hence the energies for singlet (in-phase) or doublet (anti-phase) conditions are respectively comparable with the energies at which single or double spectra are observed in photoemission in figures 21(a) and (b).

Based on this resemblance, we analyse the photoemission data of figure 21 using the wavevector plot of figure 22, which is similar to that used in spot profile analysis in LEED (SPALEED). The data points in figure 22 represent the (k_x, k_z) momentum calculated at the band bottom for Au(223) and at the centre of the $N = 1$ broad spot of Au(23 23 21) shown
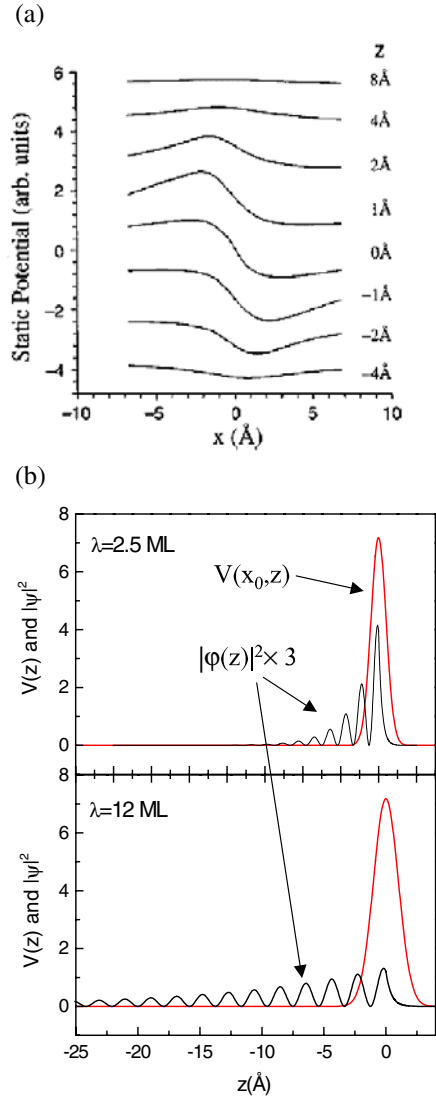
(a)

(b)

Figure 20. (a) Step potential as a function of the distance above and below the step (adapted from [5]). (b) z dependence of the step potential $V(x_0, z)$, where x_0 is the position of the step, and probability densities for two different decay lengths of surface states. The lower degree of localization of the surface resonance in the surface (bottom) leads to a lower effective potential.

in figure 10(c). k_z is calculated assuming the simplest approach for the photoemission final state [40], i.e. a free-electron-like band in an inner potential $V_0 = 15.21$ eV:

$$k_z = \sqrt{\frac{\hbar^2}{2m}(E_{\text{kin}} + V_0) - k_x^2}. \tag{11}$$

Figure 22 actually reflects the complete Fourier spectrum $(k_x, k_y = 0, k_z)$ of the surface state, which is probed by scanning the emission angle (k_x, k_y) and the photon energy (k_z). The weight of the different Fourier components is proportional to the normalized intensity of the photoemission peak, represented in figure 22(a) by the size of the dots. The shaded cigar
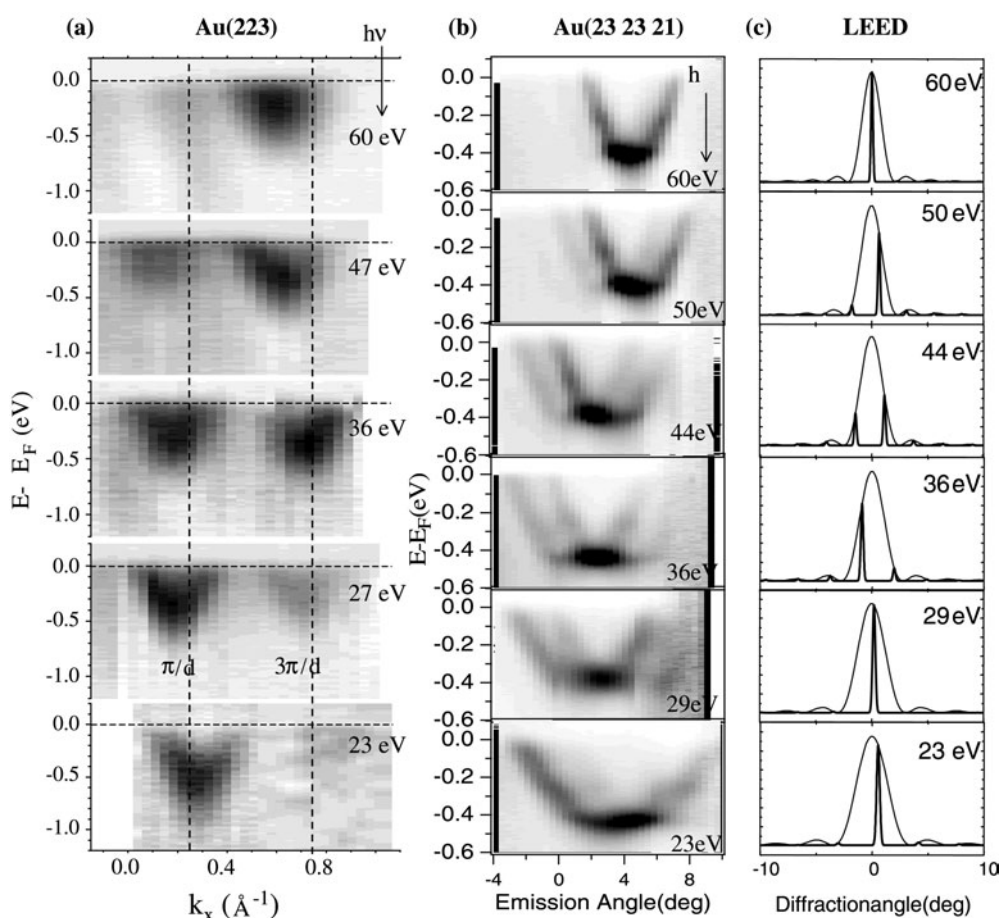
Figure 21. Spectra series for varying photon energy for (a) Au(223) and (b) Au(23 23 21). In both cases the spectra are duplicated and the relative intensity modulated in photon energy. (c) LEED calculation of a vicinal Au(111) surface for the (00) spot at normal incidence and back scattering, showing the spot splitting due to the step array.

shapes in such a figure qualitatively describe the continuous Fourier distribution of the surface state. For Au(223) this is oriented perpendicular to the surface, as expected for 2D surface states confined in the average-surface plane. As also expected for L-neck derived surface states the maximum intensity is found near the L-point of the bulk band structure, which is theoretically accessed at the points indicated in the figure [53]. The intensity modulation of the spectra for varying photon energy can be followed with the constant energy lines shown as dotted curves. From the Fourier map one can obtain the qualitative picture of the real-space wavefunction shown in the bottom panel. Along the x direction, it is composed of Bloch waves with the periodicity of the superlattice. Along the z direction, it is an evanescent oscillation with $k_z = k_L$, consistent with the k_z-broadening away from the L-point.

In contrast to the case of Au(223), the two sets of data points in figure 22(b) for Au(23 23 21) line up parallel to the [111] axis. This corresponds to the decay direction of QW wavefunctions confined in terraces, as depicted in the bottom panel. In this case the reference plane (or modulation plane) is the (111) terrace. On the other hand, data points for Au(23 23 21)
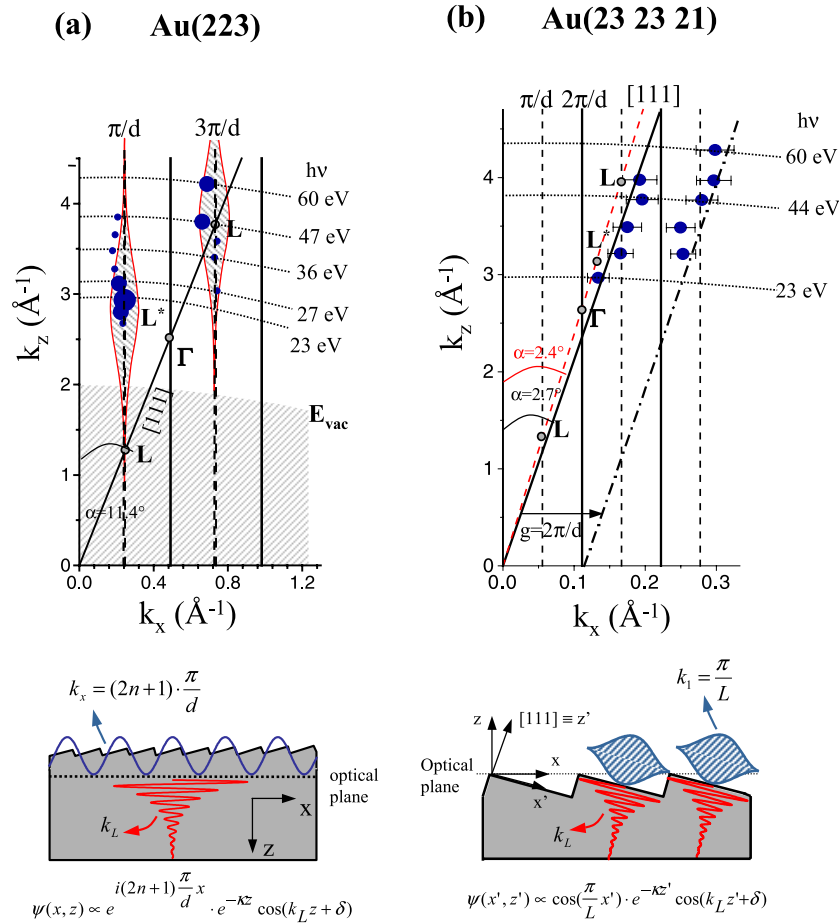
Figure 22. Diffraction plots (top) and corresponding wavefunctions (bottom) for (a) Au(223), measured at the band bottom, and (b) Au(23 23 21), measured at the centre of the $N = 1$ level. In (a) the size of the dots is proportional to the peak intensity, thereby reflecting the weighted Fourier spectrum of the surface state represented by the cigar-shaped rods (see text). The latter is broadened perpendicular to the surface, as expected for the average-surface modulated states in this case (bottom). (b) The data points for QW states in Au(23 23 21) align along the [111] direction, indicating wavefunction decay perpendicular to the terraces (bottom). Split lines in Au(23 23 21) are due to final state diffraction.

also display umklapp by step superlattice vectors. In this case, the confinement of the surface state on a single terrace discards any effect of the step array on the surface state. However, the photoemission final state is delocalized and this can undergo scattering by superlattice vectors, in the same way as LEED electrons (figure 21(c)).

6. Transition from terrace to average-surface modulation

Due to the herring-bone reconstruction, Au(111) vicinal surfaces with miscut angles between ∼4° and ∼10° undergo faceting. Thus, one cannot analyse diffraction plots at intermediate miscut angles, i.e. those between the 1D QW and the 2D step superlattice state regimes. For this purpose we perform photon-energy-dependent measurements from v-Cu(111) surfaces
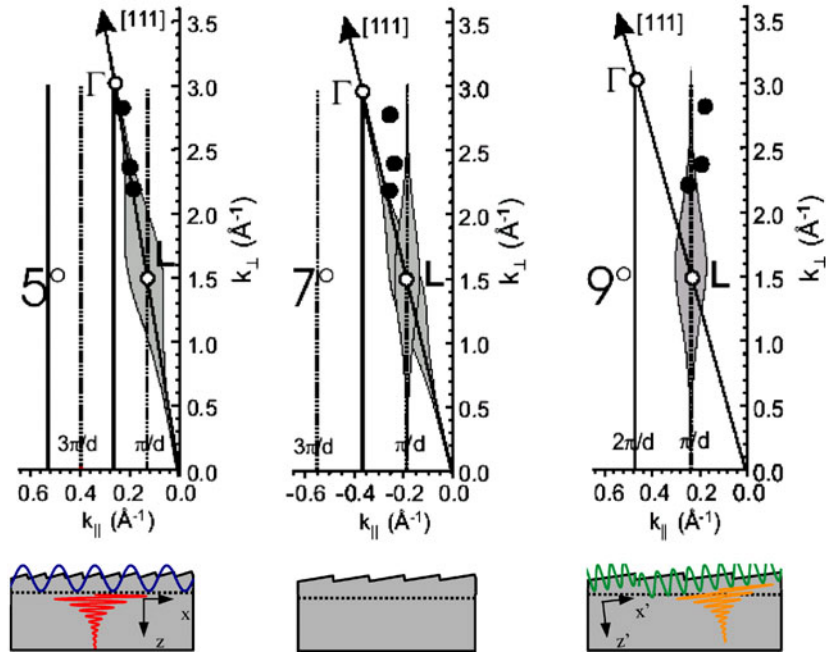
Figure 23. Diffraction plots for v-Cu $\alpha = 9°$ (left), 7° (centre) and 5° (right). The corresponding wavefunctions are plotted below.

with sharp arrays of {100}-like steps (see table 1). In figure 23 we show the diffraction plots for 5°, 7° and 9° miscuts in the top panels and the corresponding real-space wavefunction at the bottom. In all cases, the surface state displays parabolic dispersion in the direction perpendicular to the steps, discarding the presence of complete confinement within terraces, as in 1D QW states. However, a transition is observed in the alignment of the data in figure 23. For the vicinal surface with narrowest terrace width (9°, $L \sim 13$ Å) data points line up vertically, indicating average-surface modulation of the surface state. In the case of 5° miscut ($L \sim 24$ Å), in spite of the 2D character of the surface state, this is modulated on the terrace, since data points line up along the [111] direction in the diffraction plot, like the 1D QWs in figure 22(b). The shift from terrace to average-surface-like wavefunction seems to be smooth, as indicated by the data points lying between the direction perpendicular to the average surface and the [111] axis in the intermediate case of 7° miscut ($L \sim 17$ Å). Thus the transition in the modulation plane of the wavefunction occurs at $\sim 7°$, which is also the critical angle for $\bar{\Gamma}$ gap closing, as stated in the previous section.

The overall evolution of both the dimensional character (1D versus 2D) and the wavefunction type (terrace versus average-surface) of surface states at vicinal (111) noble metal surfaces can be understood within the bulk band projection picture outlined in figure 18. In figure 24 we examine the band projection also at the intermediate miscut angles of figure 23. Now we include the Fourier spectrum of the surface state determined in the diffraction plots of figures 21 and 22, which display an increasing overlap with bulk states as the gap closes. At small miscuts, the whole Fourier distribution of the surface state (the $\overline{L\Gamma}$ line) lies within the gap. As we concluded earlier, this is the reason for having a strong step potential, and hence complete confinement within terraces of 1D QW states. With 5° miscut the terrace modulation leads to full $k_\parallel$ broadening in the SBZ, such that the Fourier components of the surface state near
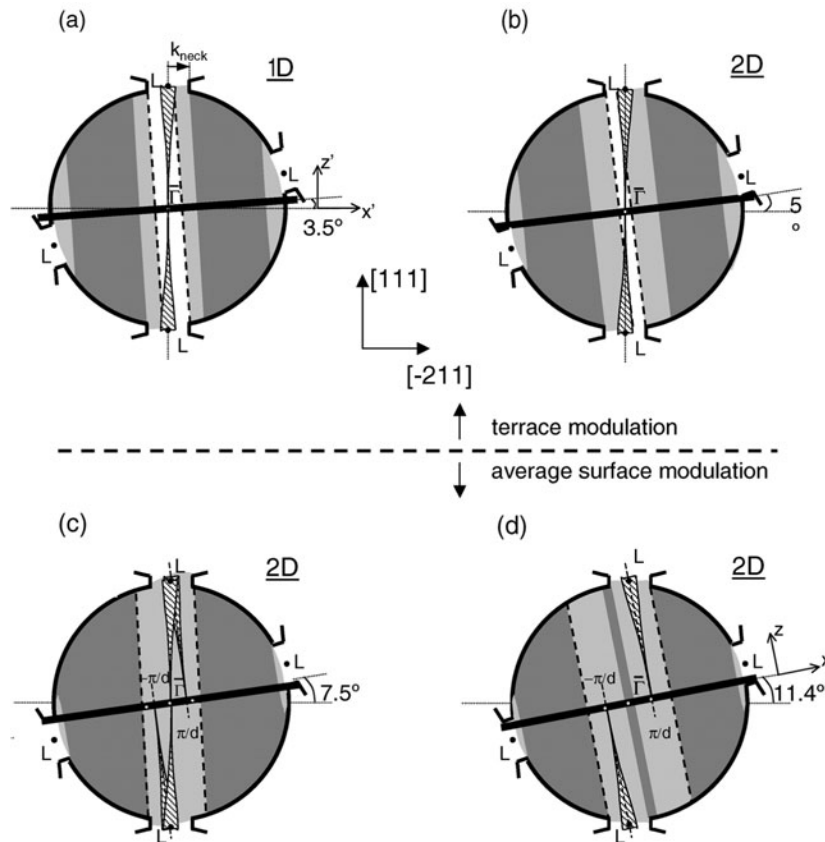
Figure 24. Bulk band projection at $E = E_F$ onto the different vicinal planes of figure 23. The cigar-shaped rods represent the momentum distribution of the surface state in the $z(z')$ direction as deduced from figures 22 and 23. The increasing overlap of the Fourier spectrum with projected bulk bands explains both the change in the dimensional character (1D versus 2D) and the switch in the modulation plane (terrace versus average-surface).

the L-point overlap with bulk states[4]. That reduces the effective step potential, as discussed previously, thereby allowing terrace-to-terrace coupling and surface band dispersion. The complete overlap at different energies occurs at a closing gap between 7° and 9° miscuts, where the smooth change in the modulation plane to average-surface-like for surface resonances is observed.

7. Wavefunction mapping

In the QW regime at very low miscuts, it is possible to go beyond the analysis of the modulation plane and the dispersing properties of the surface state. In such a case, the angle-resolved photoemission intensity variation for each quantum level (I_N) contains enough information to recover completely the respective QW wavefunction in real space. In figures 25(a) and 26(a) data points correspond to the QW peak intensity obtained from fitting a line to the spectra

[4] The angle α'_c at which the projection of the L-point falls outside the gap is (for $E = E_F$) $\alpha'_c = \tan^{-1}(k_{neck}/2k_L) = 4.9°$.
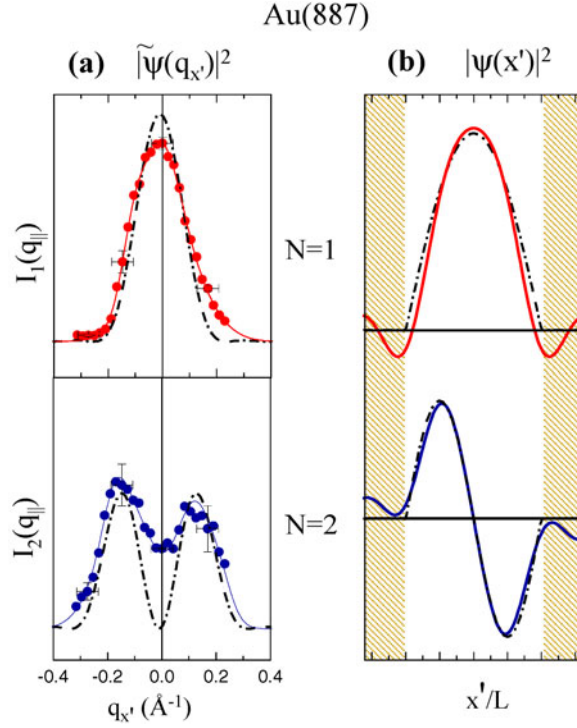
Au(887)

Figure 25. (a) Photoemission intensity of the two QW levels in Au(887) as a function of the wavevector parallel to the terrace and perpendicular to the steps (see figure 10). The thin curves are interpolation curves of the data points. The dashed curves represent the expected photoemission intensity from the infinite QW of the same width. (b) Wavefunctions corresponding to the photoemission intensities in (a) obtained by iterative oversampling (see text). The solid curves correspond to the experimental wavefunctions, and their respective infinite QW wavefunctions are represented with dashed curves.

of Au(887) and Au(23 23 21) shown in figures 10(b) and (c). For the horizontal axis we have chosen $q_{x'}$, i.e. the photoelectron parallel momentum reduced to the first SBZ. As is theoretically proved in [14], under the particular conditions of both experiments, $I_N(q_{x'})$ can be assumed to be proportional to the probability density of the electron in the quantum well:

$$I_N(q_{x'}) \propto |\tilde{\phi}_N(q_{x'})|^2 = |\langle q_{x'}|\phi_N\rangle|^2 = \left| \int dx' e^{-iq_{x'} \cdot x'} \phi_N(x') \right|^2 \qquad (12)$$

where $\tilde{\phi}_N(q_{x'})$ is the Fourier transform of the wavefunction in real space $\phi_N(x')$. The natural normalization of both the wavefunction and the measured intensity can be obtained from the Fourier transform of the intensity $I_N(q_{x'})$, which can be considered as a self-convolution of the real-space wavefunction [14]. After the normalization, the previous equation allows us to obtain $\phi_N(x')$ from the intensity in reciprocal space as

$$\phi_N(x') = \int \frac{dq_{x'}}{(2\pi)^2} e^{iq_{x'} \cdot x'} \sqrt{I_N(q_{x'})} e^{i\delta_N(q_{x'})}. \qquad (13)$$

This equation contains an unknown phase $\delta_N(q_{x'})$ that can be recovered by applying the iterative procedure called oversampling, previously proposed for x-ray diffraction [54–56]. The oversampling consists of minimizing $\phi(x')$ far outside the region where the wavefunction is confined. A confinement length $\tilde{L}$ is estimated directly from the self-convolution of
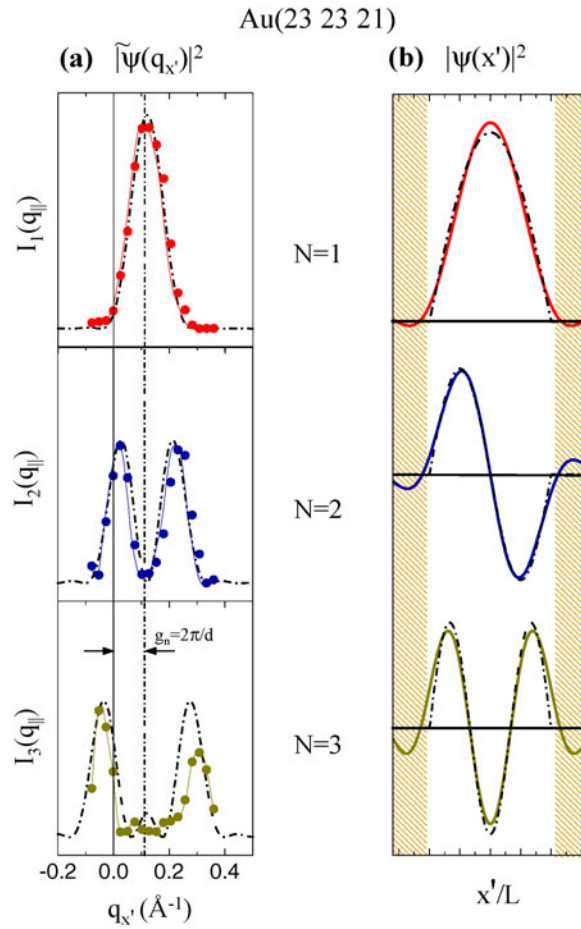
Figure 26. (a) Photoemission intensity of the three quantum levels as a function of the wavevector parallel to the terrace and perpendicular to the steps observed on Au(23 23 21) (see figure 10) and (b) corresponding wavefunctions from iterative oversampling data in (a). As in figure 10, solid curves correspond to the experimental wavefunctions, thin dotted curves are interpolation curves, and dashed curves compare the results with the infinite QW of the same width.

$\phi_N(x')$ mentioned above, and obtained by Fourier transforming the photoemission intensity $I_N(q_{x'})$. The iteration begins with a constant phase, e.g. $\delta_N(q_{x'}) = 0$, in equation (13). The resulting $\phi_N(x')$ is smoothly cut away from the 'oversampled' area, in our case by making $\phi_N = \phi_N - 0.1 \times \phi_{N-1}$ beyond $4\tilde{L}$. The resulting $\phi_N(x')$ is transformed back into $q_{x'}$ space using equation (12), and the phase of $\tilde{\phi}_N(q_{x'})$ is extracted and inserted again into equation (13) to start a new cycle. Convergence is obtained after a few hundred iterations. The results for the different quantum levels in Au(887) and Au(23 23 21) are shown in figures 25(b) and 26(b) and compared with the case of the infinite QW of size L. The wavefunctions look very similar, as expected from the comparison with probability functions in reciprocal space in figures 25(a) and 26(a). All wavefunctions are confined to a region whose width matches the terrace width L. Note that such terrace confinement has not been assumed by our reconstruction procedure, but rather it has emerged from the information contained in the photoemission data.
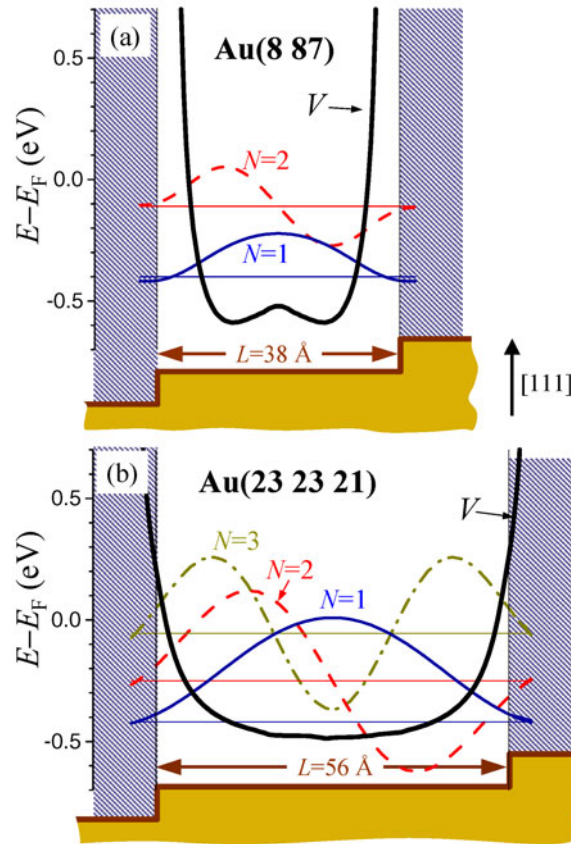
Figure 27. Experimental one-electron potentials averaged over the different QW levels observed in photoemission for (a) Au(887) and (b) Au(23 23 21). The wavefunctions are plotted together at their corresponding energy level. The step edges are represented by the coloured (vertical) walls.

From the experimental wavefunctions obtained in figures 25 and 26, we can retrieve the effective one-electron potential of the terrace from the Schrödinger equation:

$$V(x') - E_N = \frac{\hbar^2}{2m^*\phi_N(x')}\nabla^2\phi_N(x'). \tag{14}$$

From this equation we have obtained electron potentials which are basically the same for all QW levels in each surface, further confirming the correct approach. In figure 27 we show the electron potentials averaged over all QW levels. They exhibit a smooth central region and sharp boundaries that force electron confinement. It must be stressed that the validity of equation (14) is limited to regions where the wavefunction is not too small, and therefore the asymptotic limit of the step potential barrier cannot be determined. The potential barrier in both cases starts rising before the step edge is reached. For instance, the QW wavefunctions find a potential value of $V - E_0 = 0.4$ eV with respect to the reference level E_0 at ~ 5 Å and ~ 3 Å before reaching the step for Au(887) and Au(23 23 21) respectively. These 'onset' values of the potential are qualitatively comparable with the ± 2 Å estimated for the interaction length of the potential at the step from jellium models [5, 42]. Furthermore, the narrowing of the effective confinement length is consistent with the observations made by Otero *et al* [57]

in Pb islands. They relate this narrower effective potential to the electron spillover at the well boundaries.

One can use the experimental potentials to estimate the reference energy E_0. This would be given by the value of the potential in the flat region at the centre of the well. The reference energies obtained this way are $E_0 = -0.509$ and -0.486 eV for Au(887) and Au(23 23 21) respectively, in agreement with the values obtained previously from the fit to the infinite QW model.

8. Summary

Vicinal surfaces with regular arrays of steps might be viewed as model lateral nanostructures. We have measured their electronic states in detail using angle-resolved photoemission with synchrotron radiation. The latter has revealed itself as a powerful tool to study deeply electronic properties. In fact, photoemission is shown to provide the complete Fourier spectrum that allows a qualitative and quantitative probe of electron wavefunctions, either for 2D superlattice states or for 1D confined electrons. In the later case, the real-space wavefunction is exactly recovered from photoemission data using a phase-retrieval, iterative procedure borrowed from x-ray diffraction. This encourages further work using more complex 2D arrays of 1D or zero-dimensional nanostructures.

Acknowledgments

References

[1] Shapiro A P, Miller T and Chiang T-C 1988 *Phys. Rev.* B **38** 1779
[2] Sanchez O, García J M, Segovia P, Alvarez J, Vázquez de Parga A L, Ortega J E, Prietsch M and Miranda R 1995 *Phys. Rev.* B **52** 7894
[3] Wang X Y, Paiella R and Osgood R M Jr 1995 *Phys. Rev.* B **51** 17035
[4] Wang X Y, Shen X J and Osgood R M Jr 1996 *Phys. Rev.* B **53** 15738
[5] Wang X Y, Shen X J and Osgood R M Jr 1997 *Phys. Rev.* B **56** 7665
[6] Ortega J E, Speller S, Bachmann A R, Mascaraque A, Michel E G, Närmann A, Mugarza A, Rubio A and Himpsel F J 2000 *Phys. Rev. Lett.* **84** 6110
[7] Shen X J, Kwak H, Mocuta D, Radojevic A M and Osgood R M Jr 2001 *Phys. Rev.* B **63** 165403
[8] Mugarza A, Ortega J E, Mascaraque A, Michel E G, Altmann K N and Himpsel F J 2001 *Surf. Sci.* **482–485** 464
[9] Baumberger F, Gerber T and Osterwalder J 2000 *Phys. Rev.* B **62** 15431
[10] Baumberger F, Gerber T and Osterwalder J 2001 *Phys. Rev.* B **64** 195411
[11] Baumberger F, Delley B, Gerber T and Osterwalder J 2002 *Phys. Rev.* B **88** 237601
[12] Ortega J E, Mugarza A, Repain V, Rousset S, Pérez-Dieste V and Mascaraque A 2002 *Phys. Rev.* B **65** 165413

[13] Mugarza A, Mascaraque A, Repain V, Rousset S, Altmann K N, Himpsel F J, Koroteev Yu M, Chulkov E V, García de Abajo F J and Ortega J E 2002 *Phys. Rev.* B **66** 245419
[14] Mugarza A, Ortega J E, Himpsel F J and García de Abajo F J 2003 *Phys. Rev.* B **67** 081404
[15] Avouris Ph and Lyo I-W 1994 *Science* **264** 942
[16] Bürgi L, Jeandupeux O, Hirstein A, Brune H and Kern K 1998 *Phys. Rev. Lett.* **81** 5370
[17] Williams E 1994 *Surf. Sci.* **300** 502
[18] Swamy K, Bertel E and Vilfan I 1999 *Surf. Sci.* **425** 369
[19] Himpsel F J and Ortega J E 1992 *Phys. Rev.* B **46** 9719
[20] Harten U, Lahee A M, Toennies J P and Woll Ch 1985 *Phys. Rev. Lett.* **54** 2619
[21] Repain V, Berroir J M, Croset B, Rousset S, Garreau Y, Etgens V H and Lecoeur J 2000 *Phys. Rev. Lett.* **84** 5367
[22] Giesen M and Einstein T L 2000 *Surf. Sci.* **449** 191
[23] Gartland P O and Slagsvold B J 1975 *Phys. Rev.* B **12** 4047
[24] Tersoff J and Kevan S D 1983 *Phys. Rev.* B **28** 4267
[25] Courths R and Hüfner S 1984 *Phys. Rep.* **112** 53
[26] Hsieh T C, Miller T and Chiang T-C 1985 *Phys. Rev. Lett.* **55** 2483
[27] Kevan S D and Gaylord R H 1987 *Phys. Rev.* B **36** 5809
[28] Qu Z *et al* 1994 *J. Vac. Sci. Technol.* A **12** 2187
[29] McDougall B A, Balasubramanian T and Jensen E 1995 *Phys. Rev.* B **51** 13891
[30] Matzdorf R, Meister G and Goldmann A 1996 *Phys. Rev.* B **54** 14807
[31] LaShell S, McDougall B and Jensen E 1996 *Phys. Rev. Lett.* **77** 3419
[32] Matzdorf R 1998 *Surf. Sci. Rep.* **30** 153
[33] Reinert F, Nicolay G, Schmidt S, Ehm D and Hüfner S 2001 *Phys. Rev.* B **63** 115415
[34] Nicolay G, Reinert F, Hüfner S and Blaha P 2001 *Phys. Rev.* B **65** 033407
[35] Paniago R, Matzdorf R, Meister G and Goldmann A 1995 *Surf. Sci.* **336** 113
[36] Crommie M F, Lutz C P and Eigler D M 1993 *Science* **262** 218
[37] Heller E J, Crommie M F, Lutz C P and Eigler D M 1994 *Nature* **369** 464
[38] Li J, Schneider W-D, Berndt R and Crampin S 1999 *Surf. Sci.* **422** 95
[39] Kliewer J, Berndt R and Crampin S 2001 *New J. Phys.* **3** 22.1
[40] Himpsel F J 1983 *Adv. Phys.* **32** 1
[41] Abukawa T, Sasaki M, Hisamatsu F, Goto T, Kinoshita T, Kakizaki A and Kono S 1995 *Surf. Sci.* **325** 33
[42] Thomson M D and Huntington H B 1982 *Surf. Sci.* **116** 522
[43] Borland R E 1961 *Proc. Phys. Soc.* **78** 314
[44] Davis L C, Everson M P and Jaklevic R C 1991 *Phys. Rev.* B **43** 3821
[45] Himpsel F J, Ortega J E, Mankey G J and Willis R F 1998 *Adv. Phys.* **47** 511
[46] Kliewer J, Berndt R, Chulkov E V, Silkin V M, Echenique P M and Crampin S 2000 *Science* **288** 1399
[47] Hörmandiger G and Pendry J B 1994 *Phys. Rev.* B **50** 18607
[48] Crampin S, Boon N H and Inglesfield J E 1994 *Phys. Rev. Lett.* **73** 1015
[49] Crampin S and Bryant O R 1996 *Phys. Rev.* B **54** 17367
[50] Machado M, Eiguren A, Chulkov E V and Echenique P M 2003 *J. Electron Spectrosc. Relat. Phenom.* **129** 87
[51] Aballe L 2000 *PhD Thesis* Freien Universiät, Berlin
[52] Henzler M 1976 *Appl. Phys.* **9** 11
[53] Mugarza A, Ortega J E, Mascaraque A, Michel E G, Altmann K N and Himpsel F J 2000 *Phys. Rev.* B **62** 12672
[54] Saldin D K, Harder R J, Shneerson V L and Moritz W 2001 *J. Phys.: Condens. Matter* **13** 10689
[55] Miao J, Charalambous P, Kirz J and Sayre D 1999 *Nature* **400** 342
[56] Miao J, Sayre D and Chapman H N 1998 *J. Opt. Soc. Am.* A **15** 1662
[57] Otero R, Vázquez de Parga A L and Miranda R 2000 *Surf. Sci.* **447** 143
[58] Machado M 2002 private communication